Research Article

Electronic Orbital Alignment and Hierarchical Phonon Scattering Enabling High Thermoelectric Performance p-Type Mg$_3$Sb$_2$ Zintl Compounds

Jinsuo Hu,[1] Jianbo Zhu,[1] Fengkai Guo,[1] Haixu Qin,[1] Yijie Liu,[2] Qian Zhang [ID],[2] Zihang Liu [ID],[1] Wei Cai,[1] and Jiehe Sui [ID][1]

[1]*State Key Laboratory of Advanced Welding and Joining, Harbin Institute of Technology, Harbin 150001, China*
[2]*Department of Materials Science and Engineering, Harbin Institute of Technology, Shenzhen 518055, China*

Correspondence should be addressed to Zihang Liu; zihangliu@hit.edu.cn and Jiehe Sui; suijiehe@hit.edu.cn

Environmentally friendly Mg$_3$Sb$_2$-based materials have drawn intensive attention owing to their promising thermoelectric performance. In this work, the electrical properties of p-type Mg$_3$Sb$_2$ are dramatically optimized by the regulation of Mg deficiency. Then, we, for the first time, found that Zn substitution at the Mg2 site leads to the alignment of $p_{x,y}$ and p_z orbital, resulting in a high band degeneracy and the dramatically enhanced Seebeck coefficient, demonstrated by the DFT calculations and electronic properties measurement. Moreover, Zn alloying decreases Mg1 (Zn) vacancies formation energy and in turn increases Mg (Zn) vacancies and optimizes the carrier concentration. Simultaneously, the Mg/Zn substitutions, Mg vacancies, and porosity structure suppress the phonon transport in a broader frequency range, leading to a low lattice thermal conductivity of ~0.47 W m^{-1} K^{-1} at 773 K. Finally, a high ZT of ~0.87 at 773 K was obtained for Mg$_{1.95}$Na$_{0.01}$Zn$_1$Sb$_2$, exceeding most of the previously reported p-type Mg$_3$Sb$_2$ compounds. Our results further demonstrate the promising prospects of p-type Mg$_3$Sb$_2$-based material in the field of mid-temperature heat recovery.

1. Introduction

Thermoelectric (TE) devices can directly convert heat into electricity and vice versa, which can be used in waste heat recovery and refrigeration applications [1–3]. The conversion efficiency of TE devices (η) is determined by the figure of merit of materials ($ZT = S^2\sigma T/\kappa_{tot}$), where S, σ, T, and κ_{tot} are the Seebeck coefficient, electrical conductivity, absolute temperature, and total thermal conductivity, respectively. The interrelated electrical and thermal transport properties make it difficult to maintain a high power factor ($PF = S^2\sigma$) and a low thermal conductivity simultaneously [4–6]. Previously, several strategies have been proposed to optimize the power factor via band convergence [7, 8], band flatting [9, 10], and energy resonance [11, 12] or reduce the lattice thermal conductivity via grain refinement [13], dense dislocations [14, 15], and hierarchical microstructure [16–18].

Recently, Zintl phase compounds have been extensively investigated as potential mid-temperature TE materials [19–21]. Typical Zintl phases consist of electropositive cations and electronegative polyanions [22, 23]. However, the majority of them contain rare earth elements and or toxic elements, restricting the practical application [24–28]. Recently, Mg$_3$Sb$_2$-based Zintl materials have drawn wide attention because of the unique attributes of environmentally friendly, low-cost, and abundantly available constituent elements [2, 29–33]. Especially, n-type Mg$_3$Sb$_2$-based materials have demonstrated excellent TE performance due to the multivalley conduction band behavior near the Fermi level, pushing the necessity of further optimizing the performance of the p-type counterparts that currently have an inferior ZT [34–36]. Various dopants (Na, Ag, Li, Zn, Cd, and Mn at the Mg site [37–45], as well as Bi and Pb at the Sb site [46, 47]) have been reported to increase the carrier concentration and thereby improve the TE property of

p-type Mg_3Sb_2 materials. And Na is very effective for increasing the carrier concentration, but this also leads to increased lattice thermal conductivity [37, 38]. Despite these improvements, the previously reported p-type Mg_3Sb_2-based materials still display relatively low ZT values, which heavily impede its application potential. Therefore, it is crucial to further promote the TE performance of p-type Mg_3Sb_2-based materials given the prerequisite that both n- and p-type legs are required for TE devices. Previous calculations revealed that the valence band edge of Mg_3Sb_2 at the Brillouin zone center (Γ) is dominated by the p orbitals of Sb anions that are composed of $p_{x,y}$ and p_z orbital [48, 49]. The energy offset of these orbitals is determined as the crystal field splitting energy $\Delta E = E(p_{x,y}) - E(p_z)$. Intuitively, the alignment of these orbitals in the reciprocal space should be straightforward and effective to maximize the band degeneracy (N_v) and improve the electronic performance [24, 25, 50]. The TE performance enhancement has been obtained by orbital alignment in $YbZn_2Sb_2$-$YbCd_2Sb_2$, $EuZn_2Sb_2$-$EuCd_2Sb_2$, and $MgZn_2Sb_2$-$YbZn_2Sb_2$-$YbMg_2Sb_2$ Zintl compounds [24, 25, 50].

In this work, $Mg_{2.99}Na_{0.01}Sb_2$ as the base material, Mg vacancies were introduced on the basis of Na acceptor doping to maintain a high carrier concentration and decrease the lattice thermal conductivity simultaneously. More importantly, the isoelectronic substitution of Zn elements was used to manipulate the band structure (Figure 1(a)), leading to the dramatically enhanced density of states (DOS) effective mass and Seebeck coefficient. Meanwhile, the porous structure was formed during the high-temperature sintering process because part of Zn volatilizes as a consequence of its high saturated vapor pressure. The Mg/Zn substitutions, Mg vacancies, and porous structure are responsible for impeding the phonon transport and significantly decreasing the lattice thermal conductivity (Figure 1(b)). Benefited from the increased power factor and significantly decreased thermal conductivity, a high ZT value of ~0.87 at 773 K was obtained in $Mg_{1.95}Na_{0.01}Zn_1Sb_2$, exceeding most of the p-type Mg_3Sb_2 materials (Figure 1(c)) [37, 39, 40, 42, 46, 47]. Theoretically, a high predicted efficiency of ~8% was also obtained under the condition of the cold side temperature (T_c) at 300 K and the hot side temperature (T_h) at 773 K, indicating the promising prospect of our synthesized p-type Mg_3Sb_2-based materials (Figure 1(d)). Furthermore, the utilization of tuning the crystal field splitting energy and constructing hierarchical microstructure could also be applied to optimize the TE performance of other Zintl systems.

2. Results and Discussion

X-ray diffraction patterns and the calculated lattice parameters of spark plasma sintering (SPS) sintered $Mg_{2.99-x}Na_{0.01}Sb_2$ samples are shown in Figure S1. All the diffraction peaks are indexed to α-Mg_3Sb_2 with the space group of P-$3m1$ without observable impurity peaks. Besides, the change of lattice parameters calculated by the Rietveld refinement is negligible. To further confirm the phase composition,

scanning electron microscope (SEM) observations and corresponding energy dispersive spectroscopy (EDS) measurements were performed. As shown in Figure S2, the backscattered electron (BSE) SEM images of the $Mg_{2.99-x}Na_{0.01}Sb_2$ samples confirm that the samples are dense without obvious cracks, consistent with the sample's density measurement (Table S1). The actual compositions determined by EDS are listed in Table S1, and the actual compositions are slightly lower than the nominal ones. The uniform contrast in the BSE micrographs illustrates the single-phase feature when the content of Mg deficiency is less than 0.06, in agreement with the above XRD results. However, some obvious Sb-rich phases begin to appear in the sample of Mg deficiency reaching 0.06.

The temperature-dependent TE properties of $Mg_{2.99-x}Na_{0.01}Sb_2$ are shown in Figure 2. As the Mg deficiency is less than 0.06, the electrical conductivity σ increases with increasing the Mg deficiency due to the increased carrier concentration n_H, e.g., from $3.80 \times 10^{19} \, cm^{-3}$ for $Mg_{2.99}Na_{0.01}Sb_2$ sample to $7.26 \times 10^{19} \, cm^{-3}$ for $Mg_{2.95}Na_{0.01}Sb_2$ sample (Table S1). Simultaneously, the Seebeck coefficient S decreases with increasing Mg deficiency. However, when further reducing the Mg content, the anomalous change of both σ and S is due to the decreased carrier concentration n_H and carrier mobility μ_H, which may be related to the obvious precipitation of the Sb-rich phases in this sample. As a consequence of the optimization of n_H, the small fraction of Mg deficiency optimizes the electrical properties and enhances the power factor PF. Specifically, the PF of $Mg_{2.95}Na_{0.01}Sb_2$ sample reaches ~7.3 $\mu W \, cm^{-2} \, K^{-2}$ at 423 K, which is 24% higher than that of the parent material.

The total thermal conductivity κ_{tot} of samples shows a negligible change with the Mg deficiency content. To understand the phonon-scattering mechanism, the κ_{lat} is obtained by subtracting the electronic part from the κ_{tot}. The κ_{ele} can be calculated according to Wiedemann-Franz relation given by $\kappa_{ele} = L\sigma T$, where L is the Lorenz number estimated by the single parabolic band (SPB) model [51, 52]. As shown in Figure 2(e), the relationship between κ_{lat} and T is almost T^{-1}, revealing the predominance Umklapp phonon scattering. In general, the κ_{lat} is reduced with increasing the Mg deficiency owing to the strengthened point defect scattering. The κ_{lat} of $Mg_{2.95}Na_{0.01}Sb_2$ is $0.62 \, W \, m^{-1} \, K^{-1}$, which is about 14% lower than that of the parent material. Finally, we obtained the maximum ZT~0.64 at 773 K for $Mg_{2.95}Na_{0.01}Sb_2$, a 28% enhancement compared to that of $Mg_{2.99}Na_{0.01}Sb_2$. In principle, the enhanced ZT is attributed to the strengthening phonon scattering and the optimized n_H due to the Mg deficiency.

Previous work reported that the $Mg2_p$-Sb_p bonding dominates the valence band maximum (VBM) of Mg_3Sb_2 [49], and the $MgSb_4$-tetrahedron unit constitute the anionic $[Mg_2Sb_2]^{2-}$ layer. For the undistorted $MgSb_4$ tetrahedron, the equivalence of the $x, y,$ and z directions in the Brillouin zone would lead to triply degenerate p orbitals. However, since the distorted $MgSb_4$ tetrahedron in the layered Mg_3Sb_2 structure, the p_z orbital is separated from the $p_{x,y}$ orbital. To realize high band degeneracy (N_v) for enhancing electronic performance, it is relevant for the utilization of orbital
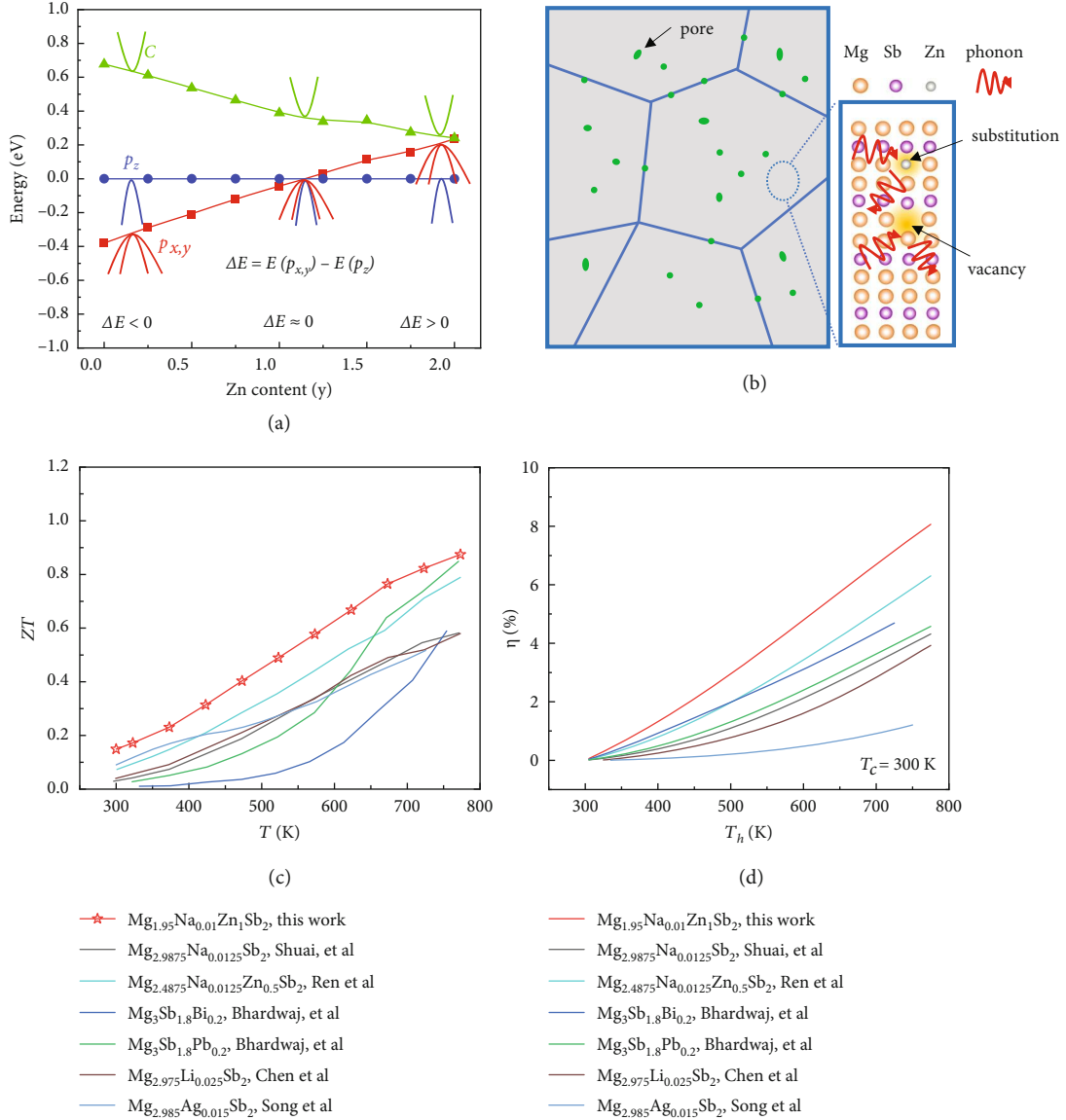
(a)

(b)

(c)

(d)

$\Delta E = E\,(p_{x,y}) - E\,(p_z)$

$\Delta E < 0$ $\Delta E \approx 0$ $\Delta E > 0$

$T_c = 300\ \text{K}$

- ☆ $Mg_{1.95}Na_{0.01}Zn_1Sb_2$, this work
- $Mg_{2.9875}Na_{0.0125}Sb_2$, Shuai, et al
- $Mg_{2.4875}Na_{0.0125}Zn_{0.5}Sb_2$, Ren et al
- $Mg_3Sb_{1.8}Bi_{0.2}$, Bhardwaj, et al
- $Mg_3Sb_{1.8}Pb_{0.2}$, Bhardwaj, et al
- $Mg_{2.975}Li_{0.025}Sb_2$, Chen et al
- $Mg_{2.985}Ag_{0.015}Sb_2$, Song et al

- $Mg_{1.95}Na_{0.01}Zn_1Sb_2$, this work
- $Mg_{2.9875}Na_{0.0125}Sb_2$, Shuai, et al
- $Mg_{2.4875}Na_{0.0125}Zn_{0.5}Sb_2$, Ren et al
- $Mg_3Sb_{1.8}Bi_{0.2}$, Bhardwaj, et al
- $Mg_3Sb_{1.8}Pb_{0.2}$, Bhardwaj, et al
- $Mg_{2.975}Li_{0.025}Sb_2$, Chen et al
- $Mg_{2.985}Ag_{0.015}Sb_2$, Song et al

FIGURE 1: (a) The calculated energy offset of $p_{x,y}$ and p_z orbitals as a function of Zn content y in $Mg_{3-y}Zn_ySb_2$. (b) Schematic view of hierarchical microstructure in $Mg_{2.95-y}Na_{0.01}Zn_ySb_2$. (c, d) Comparison of ZT values and theoretical conversion efficiency of $Mg_{1.95}Na_{0.01}Zn_1Sb_2$ with some representative p-type Mg_3Sb_2 materials [37, 39, 40, 42, 46, 47], respectively.

engineering (diminish the crystal field splitting energy of orbitals ΔE) or achieving very high n_H [48, 50].

Alloying two compounds with opposite ΔE signs could manipulate the crystal field splitting energy in 1-2-2 Zintl compounds [24, 48]. Herein, $MgZn_2Sb_2$ with opposite ΔE was chosen to alloy with Mg_3Sb_2 to tune its band structure [50], and the orbital alignment would occur in $MgMg_{2-y}Zn_ySb_2$ solid solutions. The XRD patterns of $Mg_{2.95-y}Na_{0.01}Zn_ySb_2$ samples without obvious peaks of impurities are shown in Figure S3. The EDS mapping of $Mg_{1.7}Na_{0.01}Zn_{1.25}Sb_2$ demonstrates the element homogeneity of the samples (Figure S4). The temperature-dependent electrical transport properties of $Mg_{2.95-y}Na_{0.01}Zn_ySb_2$ samples are shown in Figure 3. Upon Zn alloying, the room temperature n_H of $Mg_{2.95-y}Na_{0.01}Zn_ySb_2$ gradually increases

from $\sim 7.26 \times 10^{19}\ \text{cm}^{-3}$ $(y = 0)$ to $\sim 9.18 \times 10^{19}\ \text{cm}^{-3}$ $(y = 1.25)$ while the μ_H decreases from $\sim 62.80\ \text{cm}^2\,\text{V}^{-1}\,\text{s}^{-1}$ $(y = 0)$ to $\sim 32.34\ \text{cm}^2\,\text{V}^{-1}\,\text{s}^{-1}$ $(y = 1.25)$ (Table S1). The σ of all samples decreases with increasing temperature, and this reduction tendency becomes slow at the high-temperature range because of the thermally activated carriers. With increasing the alloying content of Zn, the σ first decreases due to the reduced μ_H and then slightly increases due to the enhanced n_H (Table S1). Room temperature σ is given in the inset of Figure 3(a) to see the difference more clearly. Considering that the S is inversely proportional to the n_H, the S should decrease with the increased n_H. However, the measured room temperature S is noticeably improved from 92 to 107 $\mu\text{V}\,\text{K}^{-1}$ after Zn alloying (as shown in the inset of Figure 3(b)). In addition, this critical temperature
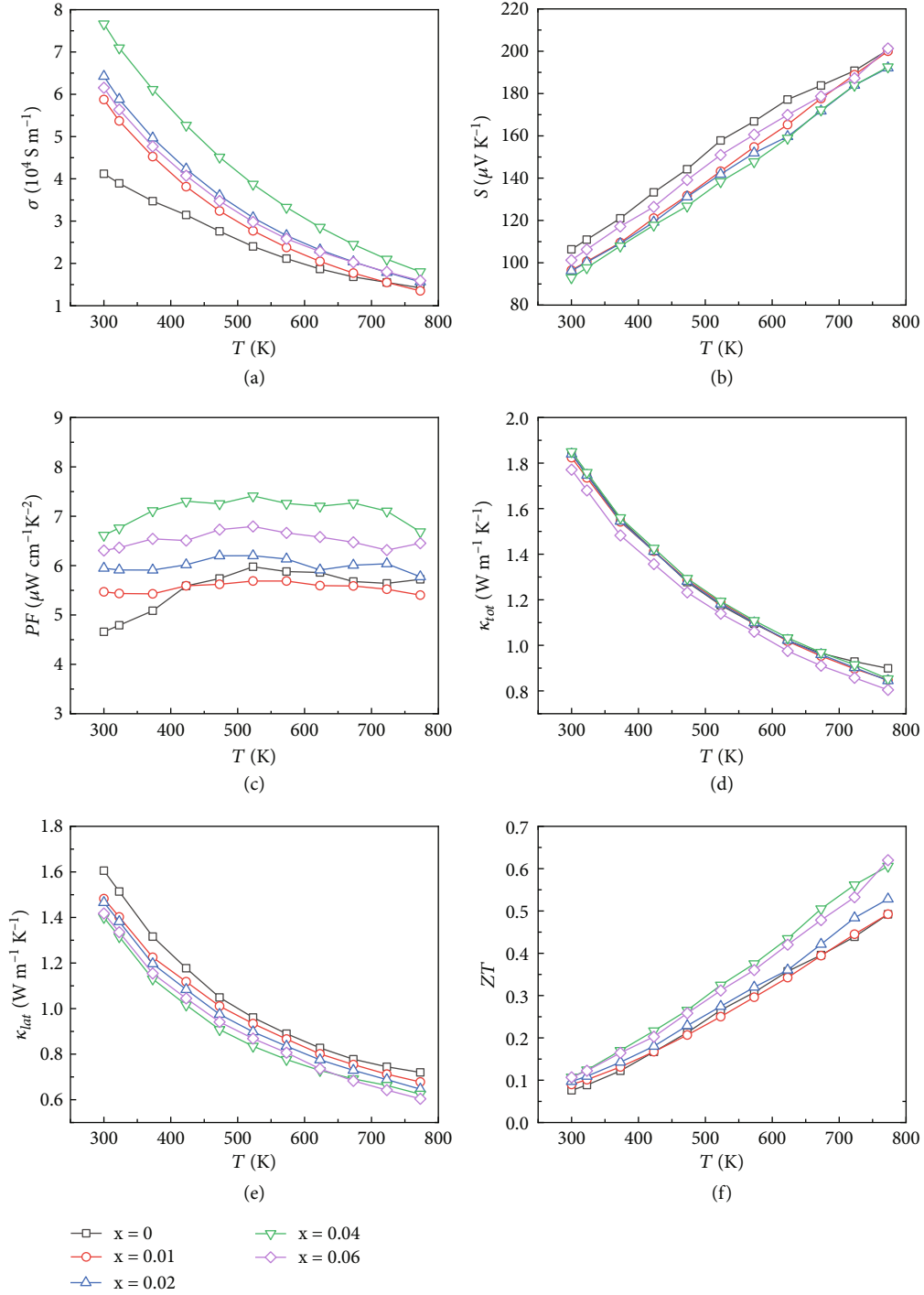
FIGURE 2: Temperature-dependent thermoelectric transport behavior of $Mg_{2.99-x}Na_{0.01}Sb_2$: (a) electrical conductivity σ, (b) Seebeck coefficient S, (c) power factor PF, (d) total thermal conductivity κ_{tot}, (e) lattice thermal conductivity κ_{lat}, and (f) figure of merit ZT.

corresponding to the occurring of the maximum S gradually shifts to the lower temperature with increasing the Zn content due to the decreased bandgap.

The SPB model, assuming acoustic phonon scattering as the main mechanism, is commonly used to describe the relationship between the S and n_H in TE field [39–41, 53–55]. The experimental data of $Mg_{2.99-x}Na_{0.01}Sb_2$ fitted well with the theoretical prediction line of $m^* = 0.75\, m_e$ based on the

SPB model and was consistent with the previous work [37, 39, 40], indicating the validity of the rigid band approximation when introducing a slight Mg deficiency. However, the experimental data of $Mg_{2.95-y}Na_{0.01}Zn_ySb_2$ are above this line, indicating that Zn alloying may change the DOS effective mass and valence band structure of Mg_3Sb_2. The DOS effective masses of $Mg_{2.95-y}Na_{0.01}Zn_ySb_2$ at room temperature calculated using the SPB model based on the

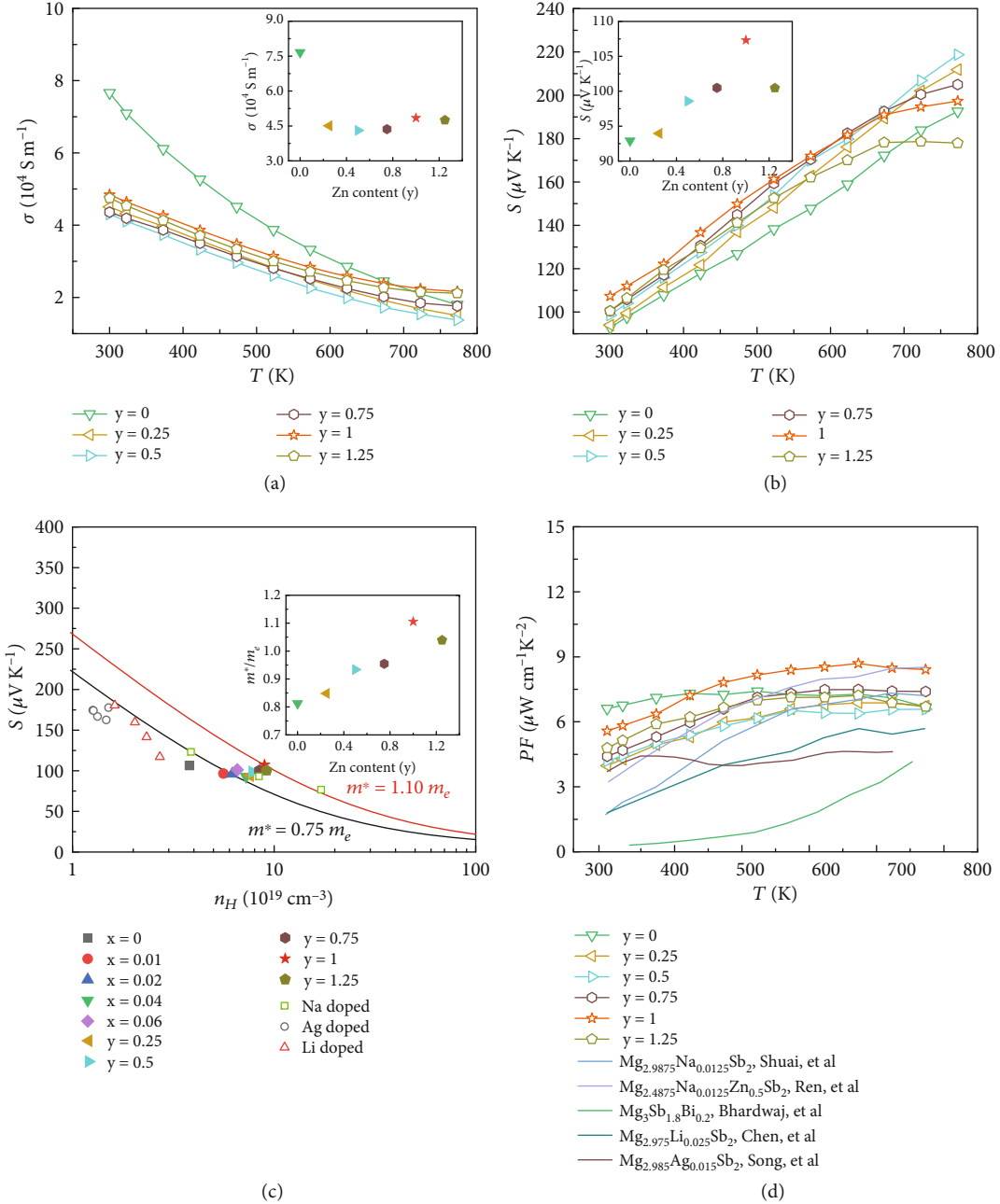FIGURE 3: Temperature-dependent electrical properties of $Mg_{2.95-y}Na_{0.01}Zn_ySb_2$: (a) electrical conductivity σ (the inset shows the room temperature electrical conductivity), (b) Seebeck coefficient S (the inset shows the room temperature Seebeck coefficient), (c) carrier concentration n_H-dependent Seebeck coefficient S of $Mg_{2.99-x}Na_{0.01}Sb_2$, $Mg_{2.95-y}Na_{0.01}Zn_ySb_2$ and the previously reported data at room temperature [37, 39, 40], where the solid line was calculated based on the SPB model (the inset shows the DOS effective mass of $Mg_{2.95-y}Na_{0.01}Zn_ySb_2$ calculated by the SPB model), and (d) temperature-dependent power factor PF of $Mg_{2.95-y}Na_{0.01}Zn_ySb_2$ and some representative p-type Mg_3Sb_2 materials [37, 39, 40, 42, 46].

experimental results are shown in the inset of Figure 3(c). The DOS effective mass gradually increases with increasing Zn doping ($y \leq 1$) which is the underlying reason for the experimentally increased S. This is due to the significant change of valence band structure after Zn alloying, leading to the increased N_v, which will be thoroughly elaborated in the following discussion. As shown in Figure 3(d), the highest PF increases from $\sim 6.7\,\mu W\,cm^{-1}\,K^{-2}$ for $Mg_{2.95}Na_{0.01}Sb_2$

to $8.4\,\mu W\,cm^{-1}\,K^{-2}$ for $Mg_{1.95}Na_{0.01}Zn_1Sb_2$ due to this beneficial band engineering.

To verify the above analysis, we calculated the band structure of $Mg_{3-y}Zn_ySb_2$, as shown in Figure 4. According to the previous work, Zn atoms are only located in the $[Mg_2Sb_2]^{2-}$ layer [56, 57]. With the increasing Zn alloying content, a heavier band contributed from $p_{x,y}$ orbital of Sb moves much closer to the VBM, so the energy difference
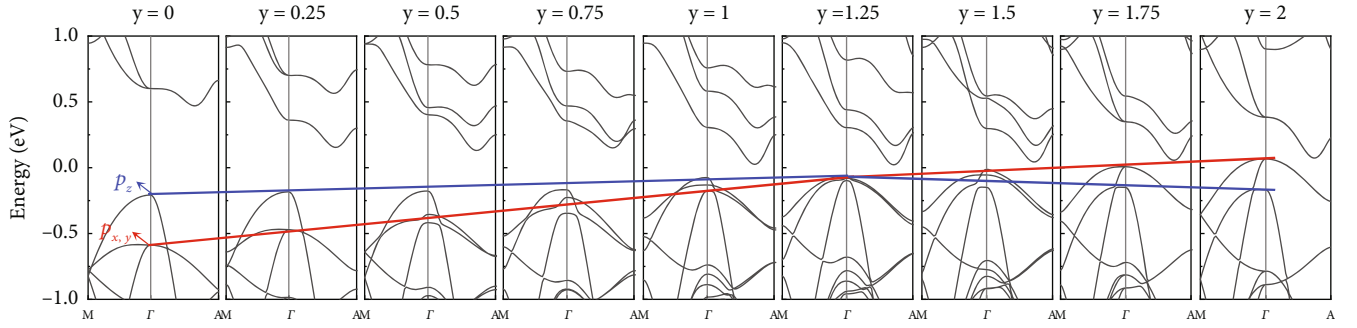
FIGURE 4: Calculated band structure of $Mg_{3-y}Zn_ySb_2$: p_z orbital gradually converges with $p_{x,y}$ orbitals until the two orbitals diverge at around $y = 1$ with the increasing Zn content (the calculated band structures are built in a $2 \times 2 \times 1$ supercell).
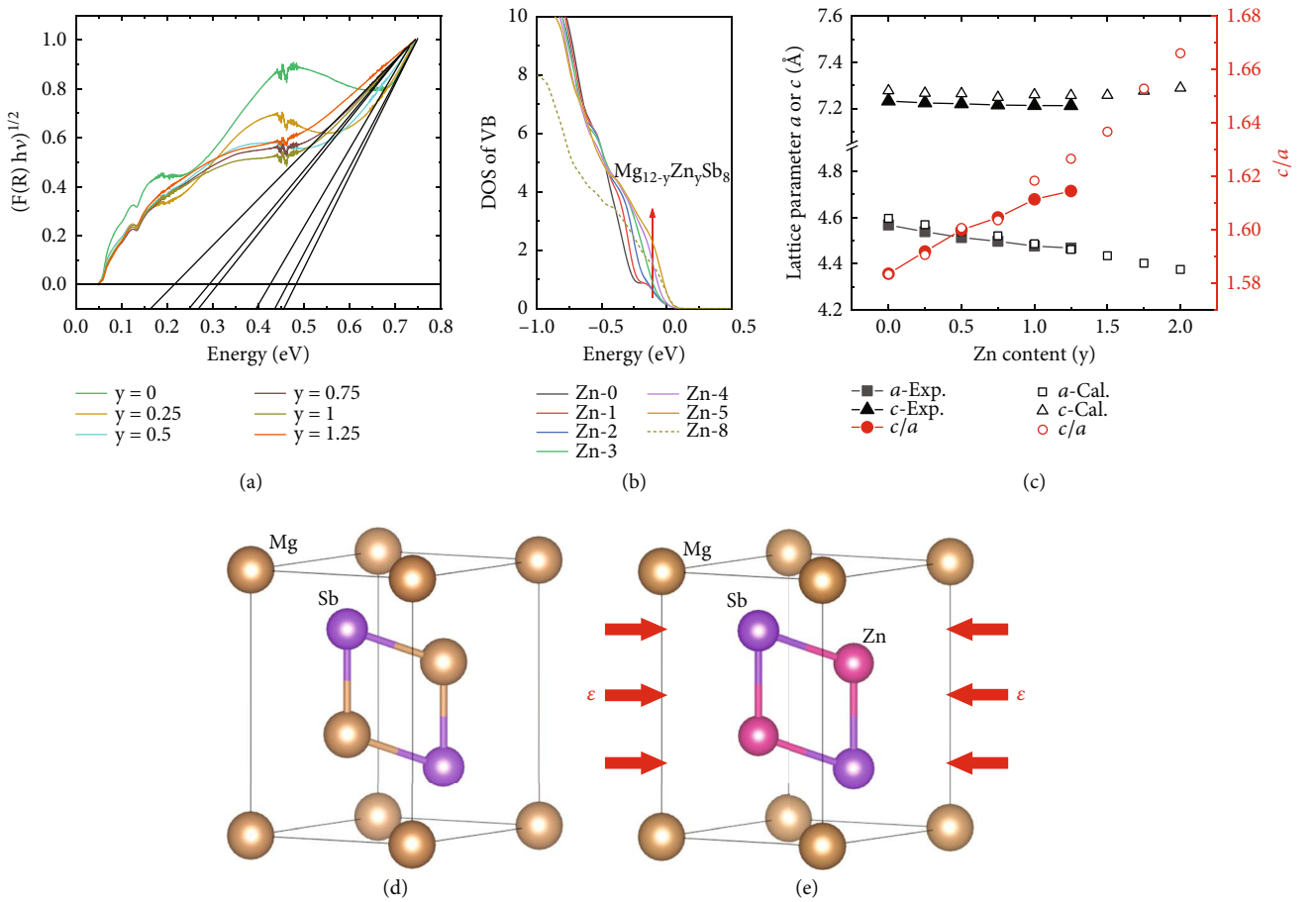

(a)

(b)

(c)

(d)

(e)

FIGURE 5: (a) Room-temperature optical absorption versus photo energy for $Mg_{2.95-y}Na_{0.01}Zn_ySb_2$. (b) The calculated DOS of $Mg_{12-y}Zn_ySb_8$. (c) The experimental and calculated lattice parameters and the ratio of c/a. (d, e) The crystal structure of Mg_3Sb_2 and $MgZn_2Sb_2$, respectively.

ΔE of $p_{x,y}$ and p_z orbitals gradually decrease until the two orbitals diverge at around $y = 1$, i.e., alignment of $p_{x,y}$ and p_z orbitals. The orbital alignment is expected to effectively increase N_v, resulting in an increased DOS effective mass and S. The negligible change μ_H after Zn alloying can be understood by compromise among the introduced defects,

involvement of the heavy $p_{x,y}$ orbital, and polarity of the anionic framework [44, 58].

According to the Fourier transport infrared (FTIR) measurement, the estimated optical band gap of $Mg_{2.95-y}Na_{0.01}Zn_ySb_2$ at room temperature is 0.48 eV, 0.46 eV, 0.42 eV, 0.31 eV, 0.29 eV, and 0.16 eV for $y = 0$, 0.25, 0.5, 0.75, 1, and

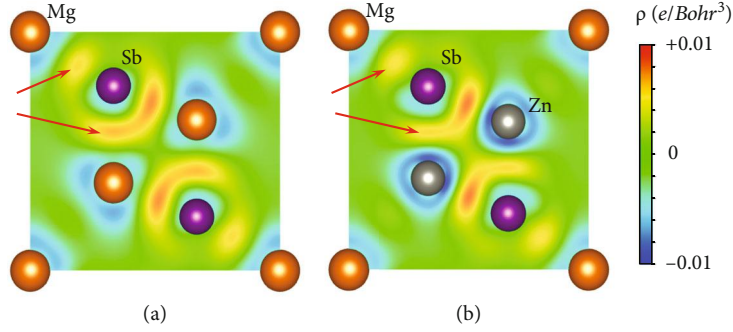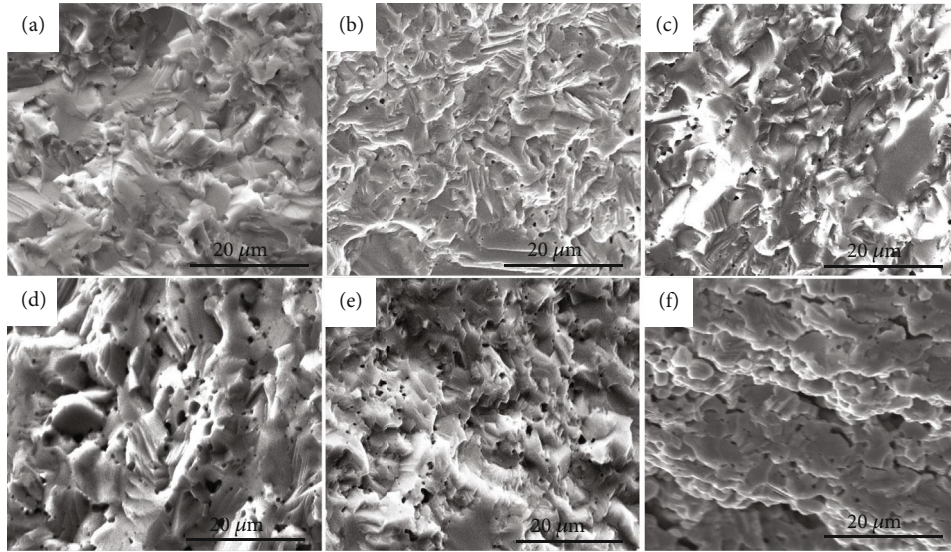FIGURE 6: The calculated deformation charge density distribution of (a) Mg_3Sb_2 and (b) $MgZn_2Sb_2$.

FIGURE 7: SEM images of $Mg_{2.95-y}Na_{0.01}Zn_ySb_2$: (a) $y = 0$, (b) $y = 0.25$, (c) $y = 0.5$, (d) $y = 0.75$, (e) $y = 1$, and (f) $y = 1.25$.

1.25, respectively (Figure 5(a) and Figure S5). The measured optical band gap as a function of Zn content is basically consistent with our previous theoretical calculation value [59, 60]. Figure 5(b) shows that the calculated DOS of $Mg_{12-y}Zn_ySb_8$ increases with the Zn content when the Zn content is less than 5, which is attributed to the gradual alignment of the $p_{x,y}$ and p_z orbitals. Then the sudden drop of DOS of $Mg_4Zn_8Sb_8$ is due to the orbital diverge (more detailed information is shown in Figure S6).

According to the previous prediction, "the reduced effect from the crystal field on the Mg2-p orbital along the z-direction would decrease the energy offset of p_z and $p_{x,y}$ orbital, and thus lead to the orbital alignment of p_z and $p_{x,y}$. Therefore, an intuitive way to achieve the orbital alignment is to enlarge the lattice parameter ratio c/a. If the atomic distance of z-direction is enlarged elongated relative to x or y, the p_z orbital would suffer a weaker crystal field effect" [49]. As shown in Figure 5(c), lattice parameters a and c decrease upon Zn doping due to the smaller atomic radius of Zn than Mg, while a change more obviously than c which is probably related to the inherently layered structure of Mg_3Sb_2 [42, 47]. This means that the compressive force is applied in

the ab plane in the Mg_3Sb_2 lattice after Zn doping (Figures 5(d) and 5(e)). According to the previous reports [48], a linear correction between crystal field splitting energy ΔE and compressive strain ε is observed in the Mg_3Sb_2 Zintl compounds. Therefore, applying the compressive biaxial strain in Mg_3Sb_2 is more effective for achieving the zero-ΔE value, which indicates that the biaxial strain could be used to manipulate the ΔE continuously. The maximum PF is obtained at the optimal strain corresponding to the minimum ΔE according to the first-principles calculations. Therefore, biaxial strain engineering is a valid way to optimize TE performance.

According to the previous work, the optimal n_H of Mg_3Sb_2 gradually increases as the applied compressive stress increases [48]. Zn alloying not only tunes the band structure but also optimizes the n_H. As shown in Figure 6, we calculated the deformation charge density distribution of Mg_3Sb_2 and $MgZn_2Sb_2$. It is obvious that a small number of electrons gathered between Mg1 and Sb, so it has the characteristic of a weak covalent bond, consistent with the previous work [20, 61]. After a part of Zn replaces at the position of Mg2, the charge accumulation between Mg1 and Sb (Zn
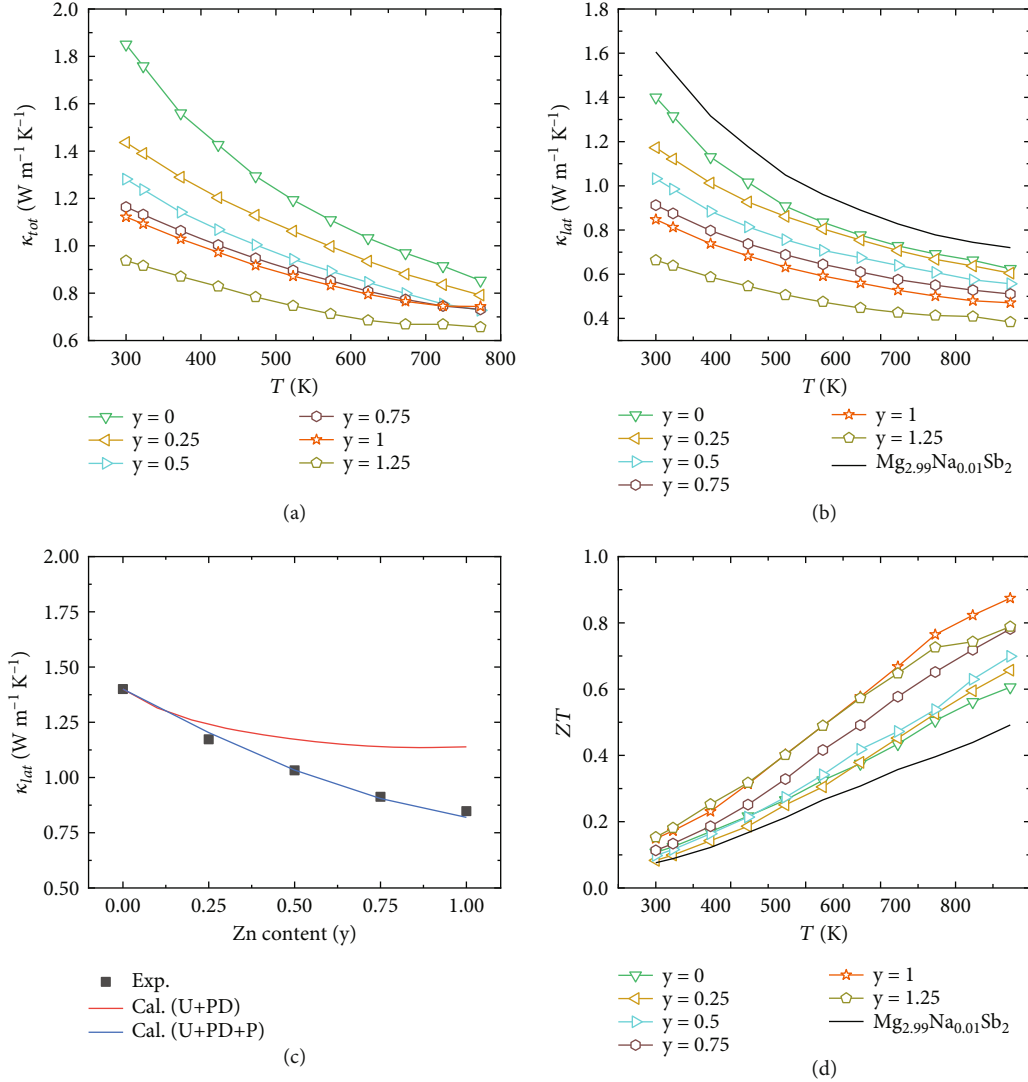
FIGURE 8: Temperature- or composition-dependent (a) total thermal conductivity κ_{tot}, (b) lattice thermal conductivity κ_{lat}, (c) lattice thermal conductivity κ_{lat} at room temperature calculated by the Callaway and Klemens model [63, 64, 66, 67], and (d) ZT values of $Mg_{2.95-y}Na_{0.01}Zn_ySb_2$.

and Sb) atoms decreases, which mean that the interaction between atoms becomes weakened. This would cause the Mg1 (Zn) atom to break the local bonding more easily to form vacancies, thereby leading to a higher n_H.

In addition to the beneficial modification on the valence band structure, the fracture surface of the $Mg_{2.95}Na_{0.01}Zn_ySb_2$ samples displays the form of brittle transcrystalline fracture with typical lamellar morphology (Figure 7). Moreover, a small number of pores with distinct shapes and different sizes (from nanometers up to a few micrometers) homogeneously distribute in the matrix, while almost no obvious pores are present in the pristine sample, consistent with the sample's density measurement. The diameter of pores size increases gradually with increasing Zn alloying content, while the decreased sample's density is the signature of the formation of pores after Zn alloying. The porous structure may be formed mainly because of part of the Zn volatilization during the high-temperature sintering process,

due to its higher saturated vapor pressure and the lower actual content compared to the nominal composition (Table S1). Meanwhile, the volatilization of Mg also plays a part in the formation of the porous structure. The excess amount of element Sb would achieve a eutectic mixture with Mg_3Sb_2 [62], so a fraction of liquid phase (Sb and Mg_3Sb_2) was squeezed from the bulk sample during the sintering process (Figure S7).

As known, isoelectronic alloying would also lead to a critical reduction of κ_{lat}, due to the strengthened phonon scattering by the introduced mass and strain fluctuations. The temperature-dependent total thermal conductivity κ_{tot} is shown in Figure 8(a). After Zn alloying, the introduced large mass and negligible strain fluctuations strengthen the point defect scattering. Thus, the κ_{tot} is significantly reduced due to the suppression of the κ_{lat} (Figure 8(b)). The κ_{lat} at 773 K reached 0.38 W m^{-1} K^{-1} in $Mg_{1.95}Na_{0.01}Zn_1Sb_2$, a 47% reduction compared to $Mg_{2.99}Na_{0.01}Sb_2$.

Under the assumption that the κ_{lat} is dominant by Umklapp and point defect scattering, the Callaway and Klemens models are widely used in TE field [63–65]. The details of the model and measured sound velocity used to calculate κ_{lat} are described in the Supporting Information. Based on the κ_{lat} of the parent compound and the measured sound velocity (v), the κ_{lat} of defected composition with alloying between can be predicted. In correspondence with the decreased κ_{lat}, the scaling parameter (u) increases with the increasing content of Zn alloying owing to the increased disorder scaling parameter (Γ_{tot}). However, the measured κ_{lat} is lower than the calculated result (Figure 8(c)) which should be attributed to additional phonon scattering from the porous structure. We further analyzed the effectiveness of pores on dampening phonon propagation based on the Callaway model [66, 67]. According to this model, the κ_{lat} is inversely proportional to the number density of pores N_p, which is consistent with our measurement. With increasing Zn alloying content, the relative density decreases; accordingly, the κ_{lat} for porous samples was gradually reduced due to the increasing number of pores. The Mg vacancies, Mg/Zn substitutions, and porosity structure are responsible for suppressing the phonon transport in a broader frequency range, which significantly diminishes the κ_{lat}. It should be noted that the porous structure strengthened the phonon scattering and reduced the lattice thermal conductivity, but the mechanical property of the samples may also be worsened.

As shown in Figure 8(d), all Zn-alloyed samples show substantially boosted ZT due to the alignment of orbitals and the strengthened phonon scattering. In particular, the ZT of $Mg_{1.95}Na_{0.01}Zn_1Sb_2$ sample reaches ~0.87 at 773 K, with an increase of ~78% compared to that of $Mg_{2.99}Na_{0.01}Sb_2$. More importantly, our synthesized sample outperforms most of the previously reported p-type Mg_3Sb_2-based materials. In addition, the good reproducibility of three synthesized $Mg_{1.95}Na_{0.01}Zn_1Sb_2$ samples is confirmed, as shown in the Supporting Information (Figure S8). Repeated tests were also carried out for the $Mg_{1.95}Na_{0.01}Zn_1Sb_2$ sample, and its TE properties show a negligible change when measuring three times (Figure S9). Indeed, the decreased bonding interaction after Zn alloying may also influence the stability of Mg_3Sb_2 material [68–70].

3. Conclusions

In conclusion, the current utilization of controlling the Mg deficiency and Zn substitution for Mg significantly enhance the TE performance of p-type Mg_3Sb_2. Tuning the Mg deficiency optimizes the carrier concentration and thereby improves the electrical properties. Zn alloying enables an effective orbital alignment for maximizing band degeneracy and optimizing electronic performance. More importantly, the Mg vacancy, Mg/Zn substitution defects, and the porous structure sufficiently suppressed the phonon transport, leading to a remarkable drop of lattice thermal conductivity. Eventually, a dramatically enhanced ZT of ~0.87 was obtained for $Mg_{1.95}Na_{0.01}Zn_1Sb_2$, outperforming most of

the previously reported Mg_3Sb_2-based materials. Our results demonstrate the effectiveness of using the strategy of orbital alignment and hierarchical structure to independently optimize the thermoelectric property of p-type Mg_3Sb_2, which may apply to other thermoelectric systems.

Data Availability

All data required to support this study are presented in the paper and the supplementary materials. Additional data are available from the authors upon reasonable request.

Conflicts of Interest

The authors declare no conflict of interest.

Authors' Contributions

J. Hu and J. Zhu contributed equally to this work.

Acknowledgments

Supplementary Materials

Experimental section: sample preparation, sample characterization, and electronic structures calculations. Figure S1: (a) X-ray diffraction patterns of $Mg_{2.99-x}Na_{0.01}Sb_2$ samples. (b) Enlarged view between 40° and 50°. (c) Lattice parameter. Figure S2: BSE images of $Mg_{2.99-x}Na_{0.01}Sb_2$: (a) $x = 0$, (b) $x = 0.01$, (c) $x = 0.02$, (d) $x = 0.04$, and (e) $x = 0.06$. Figure S3: X-ray diffraction patterns of $Mg_{2.95-y}Na_{0.01}Zn_ySb_2$ samples. Figure S4: SEM image of $Mg_{1.7}Na_{0.01}Zn_{1.25}Sb_2$ and corresponding EDS elements mapping. Figure S5: Composition-dependent optical band gap of $Mg_{2.95-y}Na_{0.01}Zn_ySb_2$. Figure S6: the calculated DOS of $Mg_{12-y}Zn_ySb_8$ ($y = 0$, 1, 2, 3, 4, 5, 6, 7, and 8). Figure S7: (a) melting-phase XRD pattern of the $Na_{0.01}Mg_{2.2}Zn_{0.75}Sb_2$ and $Na_{0.01}Mg_{1.95}Zn_1Sb_2$ samples and (b, c) the melting phase during the sintering process. Figure S8: repeated measurements on temperature-dependent TE properties of $Mg_{1.95}Na_{0.01}Zn_1Sb_2$ sample. (a) Electrical conductivity σ, (b) Seebeck coefficient S, (c) thermal conductivity κ_{tot}, and (d) figure of merit ZT. Figure S9: the repeated data of $Mg_{1.95}Na_{0.01}Zn_1Sb_2$ sample. (a) Electrical conductivity σ, (b) Seebeck coefficient S, (c) thermal conductivity κ_{tot}, and (d) figure of merit ZT. Note S1: phonon modeling studies. Table S1: the measured composition, density, relative density, carrier concentration (n_H) and mobility (μ_H) of $Mg_{2.99-x}Na_{0.01}Sb_2$ ($x = 0$, 0.01, 0.02, 0.04, and 0.06) and b) $Mg_{2.95-y}Na_{0.01}Zn_ySb_2$ ($y = 0$, 0.25, 0.5, 0.75, 1, and 1.25) samples. Table S2: the measured transverse (v_t), longitudinal

sound velocity (v_l), and number density of pores N_p used to calculate κ_{lat} based on the phonon scattering process for $Mg_{2.95-y}Na_{0.01}Zn_ySb_2$ ($y = 0$, 0.25, 0.5, 0.75, 1, and 1.25) samples. *(Supplementary Materials)*

References

[1] J. Mao, H. Zhu, Z. Ding et al., "High thermoelectric cooling performance of n-type Mg_3Bi_2-based materials," *Science*, vol. 365, no. 6452, pp. 495–498, 2019.

[2] Z. Liu, N. Sato, W. Gao et al., "Demonstration of ultrahigh thermoelectric efficiency of ~7.3% in Mg_3Sb_2/MgAgSb module for low-temperature energy harvesting," *Joule*, vol. 5, no. 5, pp. 1196–1208, 2021.

[3] X. L. Shi, J. Zou, and Z. G. Chen, "Advanced thermoelectric design: from materials and structures to devices," *Chemical Reviews*, vol. 120, no. 15, pp. 7399–7515, 2020.

[4] T. Zhu, Y. Liu, C. Fu, J. P. Heremans, J. G. Snyder, and X. Zhao, "Compromise and synergy in high-efficiency thermoelectric materials," *Advanced Materials*, vol. 29, no. 14, article 1605884, 2017.

[5] G. Tan, L. D. Zhao, and M. G. Kanatzidis, "Rationally designing high-performance bulk thermoelectric materials," *Chemical Reviews*, vol. 116, no. 19, pp. 12123–12149, 2016.

[6] T. Mori, "Novel principles and nanostructuring methods for enhanced thermoelectrics," *Small*, vol. 13, no. 45, article 1702013, 2017.

[7] Y. Pei, X. Shi, A. LaLonde, H. Wang, L. Chen, and G. J. Snyder, "Convergence of electronic bands for high performance bulk thermoelectrics," *Nature*, vol. 473, no. 7345, pp. 66–69, 2011.

[8] F. Guo, B. Cui, Y. Liu et al., "Thermoelectric SnTe with band convergence, dense dislocations, and interstitials through Sn self-compensation and Mn alloying," *Small*, vol. 14, no. 37, article 1802615, 2018.

[9] Y. Pei, A. D. LaLonde, H. Wang, and G. J. Snyder, "Low effective mass leading to high thermoelectric performance," *Energy & Environmental Science*, vol. 5, no. 7, pp. 7963–7969, 2012.

[10] Z. Huang, D. Wang, C. Li, J. Wang, G. Wang, and L. D. Zhao, "Improving the thermoelectric performance of p-type PbSe via synergistically enhancing the Seebeck coefficient and reducing electronic thermal conductivity," *Journal of Materials Chemistry A*, vol. 8, no. 9, pp. 4931–4937, 2020.

[11] J. P. Heremans, V. Jovovic, E. S. Toberer et al., "Enhancement of thermoelectric efficiency in PbTe by distortion of the electronic density of states," *Science*, vol. 321, no. 5888, pp. 554–557, 2008.

[12] G. Tan, L. D. Zhao, F. Shi et al., "High thermoelectric performance of p-type SnTe via a synergistic band engineering and nanostructuring approach," *Journal of American Chemical Society*, vol. 136, no. 19, pp. 7006–7017, 2014.

[13] B. Yu, M. Zebarjadi, H. Wang et al., "Enhancement of thermoelectric properties by modulation-doping in silicon germanium alloy nanocomposites," *Nano Letters*, vol. 12, no. 4, pp. 2077–2082, 2012.

[14] S. I. Kim, K. H. Lee, H. A. Mun et al., "Dense dislocation arrays embedded in grain boundaries for high-performance bulk thermoelectrics," *Science*, vol. 348, no. 6230, pp. 109–114, 2015.

[15] X. Meng, Z. Liu, B. Cui et al., "Grain boundary engineering for achieving high thermoelectric performance in n-type Skutter-

[16] K. Biswas, J. He, I. D. Blum et al., "High-performance bulk thermoelectrics with all-scale hierarchical architectures," *Nature*, vol. 489, no. 7416, pp. 414–418, 2012.

[17] H. Qin, J. Zhu, N. Li et al., "Enhanced mechanical and thermoelectric properties enabled by hierarchical structure in medium-temperature Sb_2Te_3 based alloys," *Nano Energy*, vol. 78, article 105228, 2020.

[18] T. Hong, D. Wang, B. Qin et al., "Band convergence and nanostructure modulations lead to high thermoelectric performance in $SnPb_{0.04}Te$-y% $AgSbTe_2$," *Physics*, vol. 21, article 100505, 2021.

[19] G. J. Snyder and E. S. Toberer, "Complex thermoelectric materials," *Nature Materials*, vol. 7, no. 2, pp. 105–114, 2008.

[20] E. S. Toberer, A. F. May, and G. J. Snyder, "Zintl chemistry for designing high efficiency thermoelectric materials," *Chemistry of Materials*, vol. 22, no. 3, pp. 624–634, 2010.

[21] M. Guo, F. Guo, J. Zhu et al., "Achieving high thermoelectric performance in rare-earth element-free $CaMg_2Bi_2$ with high carrier mobility and ultralow lattice thermal conductivity," *Research*, vol. 2020, article 5016564, 10 pages, 2020.

[22] J. Shuai, J. Mao, S. Song, Q. Zhang, G. Chen, and Z. Ren, "Recent progress and future challenges on thermoelectric Zintl materials," *Materials Today Physics*, vol. 1, pp. 74–95, 2017.

[23] K.-F. Liu and S.-Q. Xia, "Recent progresses on thermoelectric Zintl phases: structures, materials and optimization," *Journal of Solid State Chemistry*, vol. 270, pp. 252–264, 2019.

[24] X. Wang, J. Li, C. Wang et al., "Orbital alignment for high performance thermoelectric $YbCd_2Sb_2$ Alloys," *Chemistry of Materials*, vol. 30, no. 15, pp. 5339–5345, 2018.

[25] L. Zheng, W. Li, X. Wang, and Y. Pei, "Alloying for orbital alignment enables thermoelectric enhancement of $EuCd_2Sb_2$," *Journal of Materials Chemistry A*, vol. 7, no. 20, pp. 12773–12778, 2019.

[26] E. S. Toberer, C. A. Cox, S. R. Brown et al., "Traversing the metal-insulator transition in a Zintl phase: rational enhancement of thermoelectric efficiency in $Yb_{14}Mn_{1-x}Al_xSb_{11}$," *Advanced Functional Materials*, vol. 18, no. 18, pp. 2795–2800, 2008.

[27] C. Chen, Z. Feng, H. Yao et al., "Intrinsic nanostructure induced ultralow thermal conductivity yields enhanced thermoelectric performance in Zintl phase Eu_2ZnSb_2," *Nature Communications*, vol. 12, no. 1, article 5718, 2021.

[28] N. Kazem, J. V. Zaikina, S. Ohno, G. J. Snyder, and S. M. Kauzlarich, "Coinage-metal-stuffed $Eu_9Cd_4Sb_9$: metallic compounds with anomalous low thermal conductivities," *Chemistry of Materials*, vol. 27, no. 21, pp. 7508–7519, 2015.

[29] H. Tamaki, H. K. Sato, and T. Kanno, "Isotropic conduction network and defect chemistry in $Mg_{3+\delta}Sb_2$-based layered Zintl compounds with high thermoelectric performance," *Advanced Materials*, vol. 28, no. 46, pp. 10182–10187, 2016.

[30] J. Zhang, L. Song, S. H. Pedersen, H. Yin, L. T. Hung, and B. B. Iversen, "Discovery of high-performance low-cost n-type Mg_3Sb_2-based thermoelectric materials with multi-valley conduction bands," *Nature Communications*, vol. 8, no. 1, article 13901, 2017.

[31] X. Chen, H. Wu, J. Cui et al., "Extraordinary thermoelectric performance in n-type manganese doped Mg_3Sb_2 Zintl: high band degeneracy, tuned carrier scattering mechanism and

hierarchical microstructure," *Nano Energy*, vol. 52, pp. 246–255, 2018.

[32] H. Shang, Z. Liang, C. Xu et al., "N-type $Mg_3Sb_{2-x}Bi_x$ alloys as promising thermoelectric materials," *Research*, vol. 2020, article 1219461, 8 pages, 2020.

[33] A. Li, C. Fu, X. Zhao, and T. Zhu, "High-performance $Mg_3Sb_{2-x}Bi_x$ thermoelectrics: progress and perspective," *Research*, vol. 2020, article 1934848, 22 pages, 2020.

[34] J. Zhang and B. B. Iversen, "Fermi surface complexity, effective mass, and conduction band alignment in n-type thermoelectric $Mg_3Sb_{2-x}Bi_x$ from first principles calculations," *Journal of Applied Physics*, vol. 126, no. 8, article 085104, 2019.

[35] J. Zhang, L. Song, A. Mamakhel, M. R. V. Jørgensen, and B. B. Iversen, "High-performance low-cost n-type Se-doped Mg_3Sb_2-based Zintl compounds for thermoelectric application," *Chemistry of Materials*, vol. 29, no. 12, pp. 5371–5383, 2017.

[36] Z. Han, Z. Gui, Y. B. Zhu et al., "The electronic transport channel protection and tuning in real space to boost the thermoelectric performance of $Mg_{3+\delta}Sb_{2-y}Bi_y$ near room temperature," *Research*, vol. 2020, article 1672051, 12 pages, 2020.

[37] J. Shuai, Y. Wang, H. S. Kim et al., "Thermoelectric properties of Na-doped Zintl compound: $Mg_{3-x}Na_xSb_2$," *Acta Materialia*, vol. 93, pp. 187–193, 2015.

[38] J. Hu, F. Guo, M. Guo et al., "Promoted application potential of p-type $Mg_3Sb_{1.5}Bi_{0.5}$ for the matched thermal expansion with its n-type counterpart," *Journal of Materiomics*, vol. 6, no. 4, pp. 729–735, 2020.

[39] L. Song, J. Zhang, and B. B. Iversen, "Simultaneous improvement of power factor and thermal conductivity via Ag doping in p-type Mg_3Sb_2 thermoelectric materials," *Journal of Materials Chemistry A*, vol. 5, no. 10, pp. 4932–4939, 2017.

[40] C. Chen, X. Li, S. Li et al., "Enhanced thermoelectric performance of p-type Mg_3Sb_2 by lithium doping and its tunability in an anionic framework," *Journal of Materials Science*, vol. 53, no. 23, pp. 16001–16009, 2018.

[41] H. Wang, J. Chen, T. Lu et al., "Enhanced thermoelectric performance in p-type Mg_3Sb_2 via lithium doping," *Chinese Physics B*, vol. 27, no. 4, article 047212, 2018.

[42] Z. Ren, J. Shuai, J. Mao et al., "Significantly enhanced thermoelectric properties of p-type Mg_3Sb_2 via co-doping of Na and Zn," *Acta Materialia*, vol. 143, pp. 265–271, 2018.

[43] X. Tang, B. Zhang, X. Zhang et al., "Enhancing the thermoelectric performance of p-type Mg_3Sb_2 via codoping of Li and cd," *ACS Applied Materials & Interfaces*, vol. 12, no. 7, pp. 8359–8365, 2020.

[44] S. Kim, C. Kim, Y.-K. Hong et al., "Thermoelectric properties of Mn-doped Mg–Sb single crystals," *Journal of Materials Chemistry A*, vol. 2, no. 31, pp. 12311–12316, 2014.

[45] L. Huang, T. Liu, X. Mo et al., "Thermoelectric performance improvement of p-type Mg_3Sb_2-based materials by Zn and Ag co-doping," *Materials Today Physics*, vol. 21, article 100564, 2021.

[46] A. Bhardwaj, A. Rajput, A. K. Shukla et al., "Mg_3Sb_2-based Zintl compound: a non-toxic, inexpensive and abundant thermoelectric material for power generation," *RSC Advances*, vol. 3, no. 22, pp. 8504–8516, 2013.

[47] A. Bhardwaj and D. K. Misra, "Enhancing thermoelectric properties of a p-type Mg_3Sb_2-based Zintl phase compound by Pb substitution in the anionic framework," *RSC Advances*, vol. 4, no. 65, pp. 34552–34560, 2014.

[48] J. Zhang, L. Song, G. K. Madsen et al., "Designing high-performance layered thermoelectric materials through orbital engineering," *Nature Communications*, vol. 7, no. 1, article 10892, 2016.

[49] X. Tan, G.-Q. Liu, H. Hu, H. Shao, J. Xu, and J. Jiang, "Band engineering and crystal field screening in thermoelectric Mg_3Sb_2," *Journal of Materials Chemistry A*, vol. 7, no. 15, pp. 8922–8928, 2019.

[50] Z. Zhang, Y. Yan, X. Li et al., "A dual role by incorporation of magnesium in $YbZn_2Sb_2$ Zintl phase for enhanced thermoelectric performance," *Advanced Energy Materials*, vol. 10, no. 29, article 2001229, 2020.

[51] A. F. May, E. S. Toberer, A. Saramat, and G. J. Snyder, "Characterization and analysis of thermoelectric transport inn-type-Ba8Ga16−xGe30+x," *Physical Review B*, vol. 80, no. 12, article 125205, 2009.

[52] J. J. Zhu, X. Zhang, M. Guo et al., "Restructured single parabolic band model for quick analysis in thermoelectricity," *npj Computational Materials*, vol. 7, no. 1, article 116, 2021.

[53] T. Fang, X. Li, C. Hu et al., "Complex band structures and lattice dynamics of Bi_2Te_3-based compounds and solid solutions," *Advanced Functional Materials*, vol. 29, no. 28, article 1900677, 2019.

[54] T. Zhou, Z. Feng, J. Mao et al., "Thermoelectric properties of Zintl phase $YbMg_2Sb_2$," *Chemistry of Materials*, vol. 32, no. 2, pp. 776–784, 2020.

[55] J. Shuai, H. Geng, Y. Lan et al., "Higher thermoelectric performance of Zintl phases $(Eu_{0.5}Yb_{0.5})_{1-x}Ca_xMg_2Bi_2$ by band engineering and strain fluctuation," *Proceedings of National Academy of Sciences of the United States of America*, vol. 113, no. 29, pp. E4125–E4132, 2016.

[56] S.-Q. Xia, P. King, and S. Bobev, "Mg and Zn disorder in $Mg_{1.59(1)}Zn_{1.41(1)}Sb_2$," *Acta Crystallographica Section E: Structure Reports Online*, vol. 62, no. 9, pp. i184–i186, 2006.

[57] F. Ahmadpour, T. Kolodiazhnyi, and Y. Mozharivskyj, "Structural and physical properties of $Mg_{3-x}Zn_xSb_2$ (x=0–1.34)," *Journal of Solid State Chemistry*, vol. 180, no. 9, pp. 2420–2428, 2007.

[58] Z. Zhang, X. Wang, Y. Liu et al., "Balancing the anionic framework polarity for enhanced thermoelectric performance in $YbMg_2Sb_2$ Zintl compounds," *Journal of Materiomics*, vol. 5, no. 4, pp. 583–589, 2019.

[59] X. Shi, X. Zhang, A. Ganose et al., "Compromise between band structure and phonon scattering in efficient n-$Mg_3Sb_{2-x}Bi_x$ thermoelectrics," *Materials Today Physics*, vol. 18, article 100362, 2021.

[60] M. Jin, S. Lin, W. Li, X. Zhang, and Y. Pei, "Nearly isotropic transport properties in anisotropically structured n-type single-crystalline Mg_3Sb_2," *Materials Today Physics*, vol. 21, article 100508, 2021.

[61] W. Peng, S. Chanakian, and A. Zevalkink, "Crystal chemistry and thermoelectric transport of layered AM_2X_2 compounds," *Inorganic Chemistry Frontiers*, vol. 5, no. 8, pp. 1744–1759, 2018.

[62] M. Ozen, M. Yahyaoglu, C. Candolfi et al., "Enhanced thermoelectric performance in $Mg_{3+x}Sb_{1.5}Bi_{0.49}Te_{0.01}$ via engineering microstructure through melt-centrifugation," *Journal of Materials Chemistry A*, vol. 9, no. 3, pp. 1733–1742, 2021.

[63] P. G. Klemens, "Thermal resistance due to point defects at high temperatures," *Physical Review*, vol. 119, no. 2, pp. 507–509, 1960.

[64] M. Wood, U. Aydemir, S. Ohno, and G. J. Snyder, "Observation of valence band crossing: the thermoelectric properties of $CaZn_2Sb_2$–$CaMg_2Sb_2$ solid solution," *Journal of Materials Chemistry A*, vol. 6, no. 20, pp. 9437–9444, 2018.

[65] X. Zhang, H. Gu, Y. Zhang et al., "Enhanced thermoelectric properties of $YbZn_2Sb_{2-x}Bi_x$ through a synergistic effect via Bi-doping," *Chemical Engineering Journal*, vol. 374, pp. 589–595, 2019.

[66] J. Callaway and H. C. von Baeyer, "Effect of point imperfections on lattice thermal conductivity," *Physical Review*, vol. 120, no. 4, pp. 1149–1154, 1960.

[67] M. Hong, Y. Wang, S. Xu et al., "Nanoscale pores plus precipitates rendering high-performance thermoelectric $SnTe_{1-x}Se_x$ with refined band structures," *Nano Energy*, vol. 60, pp. 1–7, 2019.

[68] H. Shang, Z. Liang, C. Xu et al., "N-type $Mg_3Sb_{2-x}Bi_x$ with improved thermal stability for thermoelectric power generation," *Acta Materialia*, vol. 201, pp. 572–579, 2020.

[69] L. Song, J. Zhang, and B. B. Iversen, "Thermal stability of p-type Ag-doped Mg_3Sb_2 thermoelectric materials investigated by powder X-ray diffraction," *Physical Chemistry Chemical Physsics*, vol. 21, no. 8, pp. 4295–4305, 2019.

[70] L. R. Jørgensen, J. Zhang, C. B. Zeuthen, and B. B. Iversen, "Thermal stability of $Mg_3Sb_{1.475}Bi_{0.475}Te_{0.05}$ high performance n-type thermoelectric investigated through powder X-ray diffraction and pair distribution function analysis," *Journal of Materials Chemistry A*, vol. 6, no. 35, pp. 17171–17176, 2018.